# Direct Chemical Vapor Deposition Growth of Monolayer MoS₂ on TiO₂ Nanorods and Evidence for Doping-Induced Strong Photoluminescence Enhancement

Larionette P. L. Mawlong,[†] Kamal Kumar Paul,[‡] and P. K. Giri*,[†,‡]

[†]Centre for Nanotechnology and [‡]Department of Physics, Indian Institute of Technology Guwahati, Guwahati 781039, India

S *Supporting Information*

ABSTRACT: Herein, we demonstrate a simple technique to control the population of nonradiative trions and radiative neutral excitons in single-layer MoS₂ to enhance its photoluminescence (PL) emission by forming a core−shell heterostructure (HS) of MoS₂ on TiO₂ nanorods (NRs). The monolayer MoS₂ (1L-MoS₂) shell is grown directly on a hydrothermally grown TiO₂ NR core by chemical vapor deposition, and the HS shows a strong enhancement of PL intensity by about 2 orders of magnitude over the pristine 1L-MoS₂ at room temperature. The enhancement of PL in the HS is attributed, first, to the p-doping in the MoS₂ lattice through charge transfer from MoS₂ to TiO₂, and, second, to the radiative recombination of excitons which dominates over the nonradiative ones in the HS, as confirmed by the low-temperature PL analysis. The enhancement of PL because of the p-doping effect in the bare 1L-MoS₂ has been confirmed by the oxygen plasma treatment causing the adsorption of oxygen molecules at the defect sites of MoS₂, as revealed from the Raman and PL analyses. Our results provide a novel route to grow a core−shell HS of 1L-MoS₂ and TiO₂ NRs for the strong enhancement of excitonic PL emission, which is promising for future practical applications.
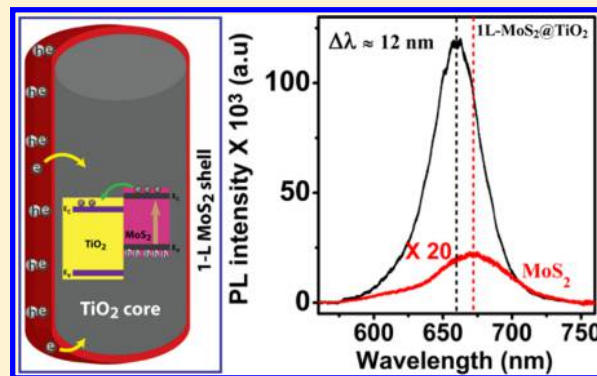
1. INTRODUCTION

Since the discovery of graphene, the two-dimensional (2D) materials have attracted much interest because of their superior optical, electrical, and mechanical characteristics. Graphene possesses extraordinary properties, including good electrical and thermal conductivity,[1,2] high carrier mobility,[3] high flexibility, and good stability. However, because of the absence of the band gap in graphene, it has severe limitations for a wider range of applications. Interestingly, the emerging semiconducting 2D transition metal dichalcogenides (TMDs) are regarded as promising candidates for these purposes. The 2D TMDs undergo a vast change in the electronic structure depending on the number of layers. Although the bulk TMDs show an indirect band gap nature, its monolayer form shows a direct band gap nature offering a great opportunity for diverse applications. The monolayer TMDs (1L-TMDs), such as MoS₂, MoSe₂, WS₂, WSe₂, and so forth, have great potential applications for future electronics and optoelectronic devices like light-emitting devices,[4,5] sensors,[6] phototransistors,[7,8] and other transistors.[9] Among the semiconducting TMDs, the monolayer molybdenum disulfide (1L-MoS₂) has drawn more research attention because of its direct band gap of ∼1.90 eV,[10,11] corresponding to the wavelength of ∼652 nm falling in the visible range, which leads to good photoluminescence (PL) and strongly enhanced optoelectronic response in its monolayer form. However, it is still a challenge to obtain high and stable PL emission from 1L-MoS₂, mainly because of the intrinsic defects leading to n-type doping.[12] Because of the strong Coulomb interaction in these confined 2D systems, the exciton in 1L-MoS₂ creates stable excitonic states even at room temperature. To control the optical properties of the 1L-TMDs, tuning the carrier density is one of the most effective methods,[12−15] realized by various methods such as electrical doping,[12,13,16] chemical doping,[14,17] and by forming vertical heterostructures (HSs) with 1L-TMDs.[18−20] The intrinsically n-type 1L-MoS₂ on further n-doping will lead to the quenching of PL, whereas p-doping will result in the PL enhancement.[12,14,17,19] With the proper utilization of the various intrinsic structural defects, such as vacancies, dislocations, grain boundaries, and edges, in both pristine/as-grown MoS₂,[21−23] tuning and improvement of the optical properties of 1L-MoS₂ is highly desirable. The commonly used SiO₂ substrate unintentionally dopes 1L-MoS₂ to an n-type layer, increases the population of trions, and thus leads to PL quenching.

By interfacing 1L-MoS₂ with other materials (plasmons, TMDs, etc.), the PL intensity can be tuned.[19,24−26] MoS₂-based nanoheterostructures with large band gap (UV-active) semiconductors, like ZnO and TiO₂, are widely reported to

form type-II heterojunctions at their interfaces, facilitating the charge separation and low PL emission. Particularly, the MoS₂/TiO₂ nanocomposite exhibits excellent combined optical properties, high chemical stability, and their availability in nature. Thus, these type-II HSs are highly promising for the applications in many fields, such as photoelectric devices, photocatalysis, energy conversion, and environmental applications.[27−35] However, most of these studies have reported on the growth of multilayer MoS₂ on TiO₂, typically grown by wet chemical methods. In these kinds of HSs, the PL emission is very low because of the indirect band gap of the multilayer MoS₂.[36] Kim et al.[36] have recently grown ZnO thin-film-based HS with 1L-MoS₂ and demonstrated a PL enhancement up to ∼17 times over the pristine 1L-MoS₂. This enhancement was explained on the basis of the conversion of trions to neutral excitons because of the charge exchanges through the interfaces, which induces p-doping in the MoS₂ lattice. They prepared ∼50 nm thick ZnO film on the quartz substrate by the sol−gel method and made the heterojunction with the chemical vapor deposition (CVD)-grown 1L-MoS₂ film after transferring it through the typical wet transfer method. However, the transfer method may introduce additional defects and impurities in the 2D material, which is often not desirable.

Here, we report a simple one-step direct synthesis process of the 1L-MoS₂ film by CVD method over the hydrothermally prepared TiO₂ nanorods (NRs). The PL intensity of 1L-MoS₂ is drastically enhanced after the formation of the HS. This enhancement is understood as a consequence of p-doping and the conversion of trions to neutral excitons. The PL and Raman spectra showed the p-doping effect that occurred through the charge transfer between 1L-MoS₂ and the TiO₂ NRs. For further verification about the p-doping in the MoS₂ lattice, a mild oxygen plasma was used to treat the samples, which confirms the doping through the oxygen bonding and charge transfer between MoS₂ and the TiO₂ interface.

2. EXPERIMENTAL PROCEDURE

2.1. Preparation of Vertically Aligned TiO₂ NRs on FTO Substrate. In a typical synthesis, 25 mL of Milli-Q water was mixed with 25 mL of concentrated hydrochloric acid (HCl) (36.5 to 38% by weight) to reach a total volume of 50 mL in a Teflon-lined stainless steel autoclave (model: BR100, Berghof Instrument Co.). The mixture was stirred at ambient conditions for 5 min before the addition of 1 mL of titanium butoxide (97%, Sigma-Aldrich). After stirring for another 5 min, one piece of fluorine-doped tin oxide (FTO) substrate (dimension ≈ 1 cm × 4 cm, surface resistivity ≈ 7 Ω/mm², Sigma-Aldrich), ultrasonically cleaned for 60 min in a mixed solution of deionized water, acetone, and 2-propanol with a volume ratio of 1:1:1, was placed at an angle against the wall of the Teflon-liner with the conducting side facing down. The hydrothermal synthesis was conducted at 150 °C for 17 h in an autoclave. Finally, the autoclave was allowed to cool naturally to room temperature and the FTO substrate was taken out, rinsed extensively with deionized water, and allowed to dry in ambient air to get a uniformly coated TiO₂ film on the FTO substrate.

2.2. Growth of 1L-MoS₂ Shell Over TiO₂ NRs. Monolayer- to few-layer MoS₂ were directly grown on the TiO₂ NRs using a two-zone furnace CVD system. Commercially procured high-purity MoO₃ (99.5%, Sigma-Aldrich) and sulfur powder (99.95%, Sigma-Aldrich) were used as precursors for the CVD growth of MoS₂ in a 2 in. quartz tube-based horizontal muffle furnace. High-purity argon (Ar) gas was used as the carrier gas. Note that both S (200 mg) and MoO₃ (15 mg) precursors were separately loaded in two ceramic boats. The typical temperatures for the source S, MoO₃, and substrates are 150, 550−600, and 700 °C, respectively. An FTO glass substrate with TiO₂ coating was mounted on top of the boat containing the MoO₃ precursor facing downward, and it was assisted from the bottom by two quartz strips, as shown in Figure S1 (Supporting Information).[37] Another ceramic boat containing sulfur powder was kept at a comparatively lower temperature zone of the furnace. The sulfur boat to MoO₃ boat distance was maintained to be 15 cm. The quartz tube inside the furnace was purged with Ar gas at 300 sccm for 30 min before the growth to remove the surface-adsorbed impurities, followed by heating up to 150 °C for another 30 min. Subsequently, the flow rate was reduced to 10 sccm, and the temperature was ramped at a rate of 15 °C/ min up to 700 °C and was maintained for 5 min. At this stage, the temperature at the sulfur boat position reached 150 °C. The furnace was then allowed to cool at 6.5 °C/min till the temperature goes down to room temperature. Interestingly, the 1L-MoS₂ film was observed to be deposited only on the portions of the substrate which were covered by the quartz mask.[37]

2.3. Characterization Techniques. The crystal structure of the as-grown samples has been obtained from X-ray diffraction (XRD) pattern (Rigaku RINT 2500 TTRAX-III, Cu kα radiation). Crystallinity, number of layers, phase, defects, and so forth in the as-grown MoS₂, as well as the phase composition and crystallinity of the as-synthesized TiO₂ NRs, have been studied by high-resolution micro-Raman spectroscopy (LabRam HR800, Jobin Yvon) with an excitation wavelength (λ_{ex}) of 488 nm (Ar ion laser). The excitation laser light was focused with a 100× objective lens to a spot size of 1 μm, with a laser power of 1.5 mW, which discards the possibility of laser heating-induced damage, and the signal was collected by a charge-coupled device in a backscattering geometry sent through a multimode fiber grating of 1800 grooves mm⁻¹. The morphology, size, and the microstructural properties of the as-synthesized TiO₂ NRs have been studied by a field emission scanning electron microscope (FESEM) (Sigma, Zeiss). The high magnification surface morphology and structures of the pristine MoS₂ and MoS₂@TiO₂ HS have been studied by a transmission electron microscope (TEM) (JEOL-JEM 2010 operated at 200 kV). The samples for TEM analysis have been prepared on a carbon-coated Cu grid of 400 mesh size (Pacific Grid, USA). The UV−vis diffuse reflectance spectroscopy (DRS) measurements of the samples were recorded using a commercial spectrophotometer (PerkinElmer, UV win Lab). Some of the MoS₂@TiO₂ HS samples were exposed to oxygen plasma at a low power (18 W) (Harrick plasma, USA).

3. RESULTS AND DISCUSSION

3.1. Morphology Studies. The typical morphology and microstructural properties of the as-grown TiO₂ NRs were first characterized by FESEM. Figure 1a depicts the top-view FESEM image of pure rutile TiO₂ NRs with a diameter of ≈ 153 ± 25 nm and a length of ≈ 835 ± 70 nm, whereas the inset shows its enlarged view, which reveals the nearly vertical growth of NRs with a uniform diameter. Figure 1b shows the cross-sectional view of vertical TiO₂ NRs grown on the FTO
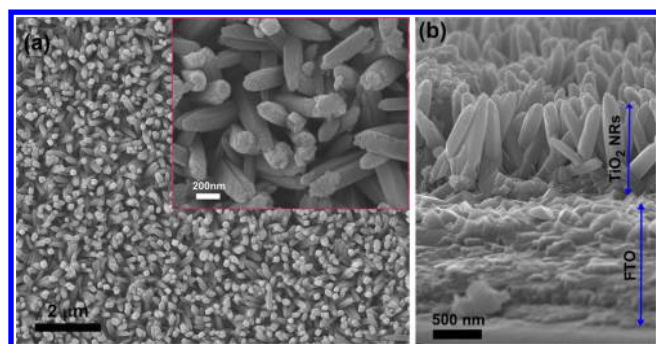
Figure 1. FESEM images of pristine TiO$_2$ NRs: (a) top view and (b) cross-sectional view. The inset in (a) shows the enlarged view of the TiO$_2$ NRs.

substrate. Considering the as-grown TiO$_2$ NR as a substrate, large-area 1L- MoS$_2$ has been grown further over it via a CVD method. The as-grown 1L- MoS$_2$ shell over the TiO$_2$ core is atomically thin and thus hard to resolve by the FESEM technique.

FETEM was employed for further characterization of the structures and surface morphologies of the HSs. The TiO$_2$ NRs possess a broad distribution in diameter of 90−290 nm. Figure 2a depicts a typical FETEM image of a TiO$_2$ NR with a diameter of ∼200 nm and length ≈ 1 μm, which is in good agreement with the FESEM analysis. Figure 2b represents the enlarged view of the top portion of the TiO$_2$ NR. The high-resolution transmission electron microscopy (HRTEM) lattice fringe pattern of TiO$_2$ of the marked region in Figure 2b is shown in Figure 2c. The lattice fringe spacing of 0.32 nm corresponds to the lattice constant of the (110) planes (see Figure 2c). The TEM image in Figure 2d,e shows a shell of 1L-MoS$_2$ over the TiO$_2$ NR core, confirming the core−shell growth of the MoS$_2$@TiO$_2$ HS. From the HRTEM image of MoS$_2$@TiO$_2$ HS, as shown in Figure 2f, it is observed that the MoS$_2$ shell thickness is ∼0.60 ± 0.02 nm, which corresponds to 1L-MoS$_2$. To further confirm the surface covering of 1L-MoS$_2$ as the shell over the TiO$_2$ NRs as the core, scanning

TEM (STEM) analysis and energy-dispersive X-ray spectrometry (EDS) mapping of the MoS$_2$@TiO$_2$ HS were conducted. The EDS pattern of MoS$_2$@TiO$_2$ HS shows that the system is composed of Ti, O, Mo, and S, as expected. Figure 3a shows a STEM image of MoS$_2$@TiO$_2$ HS on which elemental mapping analysis was performed. The EDS elemental mapping reveals that the core of the HS is composed of Ti and O elements, as shown in Figure 3b,c, whereas Figure 3d,e exhibits the elemental mapping for Mo and S, respectively, which supports our assertion that a continuous MoS$_2$ film grows over the TiO$_2$ platform as an outer layer. Figure 3f shows the corresponding atomic percentage of all the elements, which clearly reveals the presence of S-vacancy in MoS$_2$ within the HS sample.

3.2. Structural Analysis. *3.2.1. XRD Analysis.* The XRD patterns were recorded to confirm the structure, phase, and crystallinity of MoS$_2$, TiO$_2$, and their HSs, as shown in Figure S2 (Supporting Information). No diffraction pattern was detected for the atomically thin pristine 1L-MoS$_2$, but for few-layer MoS$_2$ only one peak (labeled with a "*" mark) was observed at 2θ ≈ 14.3°, which can be ascribed to the (002) planes of MoS$_2$. The hexagonal MoS$_2$ with $a = b = 0.316$ nm and $c = 1.230$ nm is in good agreement with the JCPDS card no. 37-1492. All the XRD peaks for TiO$_2$ NRs (labeled with a "♦" mark) match the standard peak value with the rutile phase of TiO$_2$ (JCPDS card no. 78-1510). The additional peaks detected in the TiO$_2$ system correspond to the standard FTO peaks, labeled with a "●" mark. It is noteworthy that no diffraction peak is detected in case of 1L-MoS$_2$@TiO$_2$ HS, which may be due to the atomically thin MoS$_2$ shell (thickness ≈ 0.60 nm) on the TiO$_2$ NRs, as evidenced by the HRTEM and Raman analyses.

3.2.2. Raman Analysis. Micro-Raman measurements were performed on the as-synthesized 1L-MoS$_2$, vertical TiO$_2$ NRs, and 1L-MoS$_2$@TiO$_2$ core−shell HS, grown on an FTO-coated glass substrate. Figure 4a represents the comparison of the Raman spectra for the samples. The growth of 1L-MoS$_2$ in both the pristine MoS$_2$ and MoS$_2$@TiO$_2$ HS is evidenced from the frequency difference (Δk) of the characteristic Raman bands (E$_{2g}$ and A$_{1g}$), which are estimated to be 19.94 and
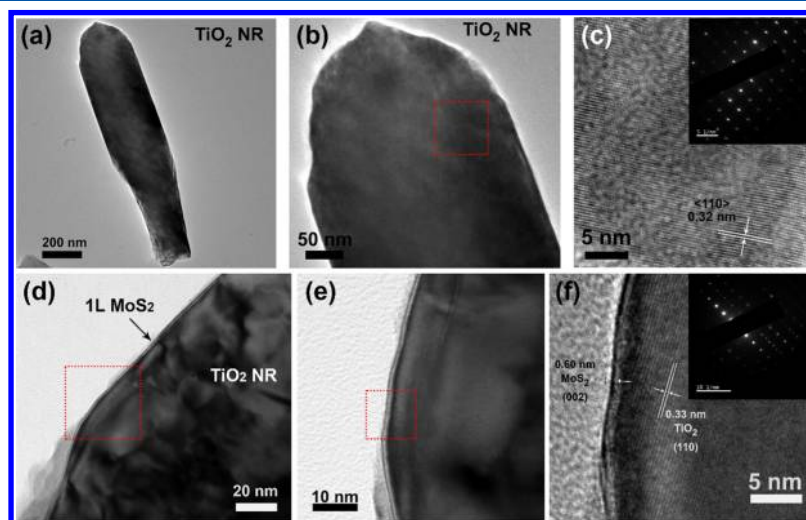

Figure 2. (a) TEM image of a TiO$_2$ NR, (b) its enlarged view, (c) HRTEM lattice fringe pattern of the selected region for TiO$_2$ NR shown in (b). Inset in (c) shows the corresponding SAED pattern. (d) TEM image of TiO$_2$ NR having a 1L-MoS$_2$ shell over it, (e) magnified view of the selected region for 1L MoS$_2$ on TiO$_2$ NR shown in (d), (f) HRTEM lattice fringe pattern of MoS$_2$@TiO$_2$ HSs at the selected region shown in (e). The inset shows the corresponding SAED pattern.
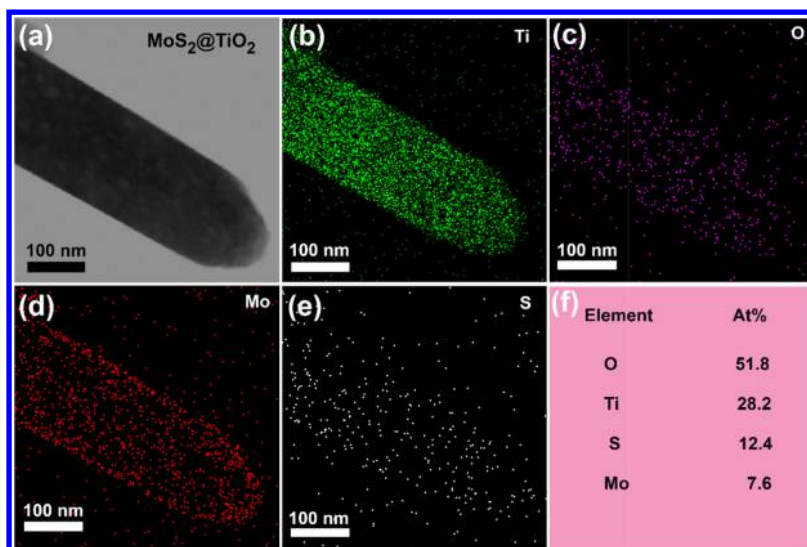
Figure 3. (a) STEM image of 1L-MoS$_2$@TiO$_2$ HS. STEM−EDX elemental mapping of different elements in the core−shell 1L-MoS$_2$@TiO$_2$ HS: (b) Ti, (c) O, (d) Mo, and (e) S. (f) Atomic percentage of the respective elements in the HS.
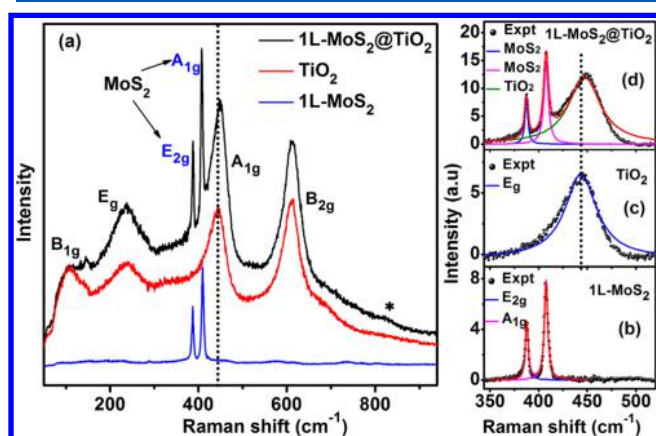

Figure 4. (a) Comparison of the Raman spectra of pristine 1L-MoS$_2$, TiO$_2$ NRs, and 1L-MoS$_2$@TiO$_2$ HS. (b−d) Lorentzian fittings of the spectra in the range of 340−520 cm^{-1} for the pristine 1L-MoS$_2$, TiO$_2$ NRs, and 1L-MoS$_2$@TiO$_2$, respectively. The symbol "*" indicates the additional peak corresponding to the O−Mo−O bonding. The vertical dotted line in each case shows the blue shift in the E$_g$ Raman band of TiO$_2$.

20.80 cm^{-1}, respectively (see Table 1 and Figure S3, Supporting Information). Both the pristine MoS$_2$ and its HS exhibit two major characteristic Raman modes of MoS$_2$: E$_{2g}$ and A$_{1g}$, associated with the in-plane vibration of two S atoms with respect to the Mo atoms and out-of-plane vibration of only S atoms in opposite directions with respect to the Mo atoms, respectively.[38] For pure rutile TiO$_2$, there are three Raman-active phonon vibrational modes at 237, 442 and 610 cm^{-1}, corresponding to the B$_{1g}$, E$_g$, and A$_{1g}$ modes, respectively. The Raman spectrum of HS is composed of the

Raman peaks of both MoS$_2$ and TiO$_2$, confirming their coexistence in the HS. Lorentzian line shape was fitted for the E$_{2g}$ and A$_{1g}$ bands of 1L-MoS$_2$ and E$_g$ band of TiO$_2$ for both cases, as shown in Figure 4b−d. The E$_g$ mode, a major characteristic Raman mode for TiO$_2$, shows a blue shift by 2 cm^{-1} in the HS with respect to that of the pristine TiO$_2$ NRs, which may be due to the compressive lattice strain induced by the coated 1L-MoS$_2$ film over its surface as an outer layer.[28] The doping state of 1L-MoS$_2$ is also known to be represented by the A$_{1g}$ mode because of the strong electron−phonon coupling along the c-axis.[14,36,38] Here, we observed a relative blue shift of the A$_{1g}$ peak of 1L-MoS$_2$ in the HS by ∼0.8 cm^{-1} with respect to that of the pristine 1L-MoS$_2$, whereas a negligible shift was detected in the E$_{2g}$ peak. It can be inferred that the shift in the A$_{1g}$ mode is due to the decrease in the electron density, which may be caused by the electron depletion through the interfaces of the HS,[39] causing the p-doping effect in 1L-MoS$_2$ in the HS. There is an additional peak appearing at 821 cm^{-1} in the HS of the Raman spectrum (see Figure 4a, marked with "*") which may be attributed to the O−Mo−O bonding.[40]

3.3. Optical Analysis. *3.3.1. UV−Vis Absorption Study.* To investigate the optical absorption spectra, the as-prepared samples were analyzed by UV−visible DRS. Figure 5 shows the Kubelka−Munk (K−M) function $F(R)$ of the respective samples corresponding to their reflectance spectra. The inset shows the magnified view of the spectra in the selected region of 560−720 nm, clearly revealing the different absorbance modes of MoS$_2$. The spectrum for the pristine few-layer MoS$_2$ shows the intrinsic A and B excitonic absorption bands at 663.5 and 609 nm, respectively.[30] In addition, we can clearly observe the C peak at 431.4 nm as well as the D peak at 287.4

Table 1. Summary of the MoS$_2$ Raman Modes, Their Separation (Δk) and Relative Contributions of the Different Excitonic/Trion Peaks Obtained from the Gaussian Deconvolution of PL Spectra of 1L-MoS$_2$ and 1L-MoS$_2$@TiO$_2$ HS

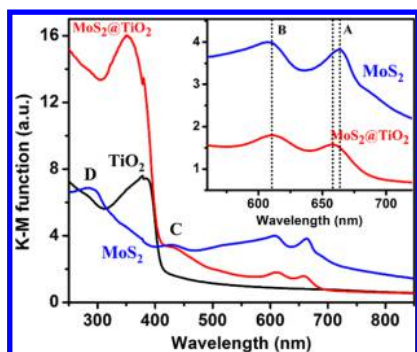|	Raman modes			relative integrated area of PL peaks			
sample	E$_{2g}$ (cm^{-1})	A$_{1g}$ (cm^{-1})	Δk (cm^{-1})	B-exciton (B) (%)	A-exciton (A) (%)	trion (A$^-$) (%)	bound exciton (X) (%)
1L-MoS$_2$	387.5 ± 0.2	407.4 ± 0.9	19.9	18.5 ± 0.7	40.8 ± 0.1	23.3 ± 0.5	17.4 ± 4.7
1L-MoS$_2$@TiO$_2$	387.4 ± 4.8	408.2 ± 2.3	20.8	11.6 ± 0.2	76.3 ± 0.2	0	12.1 ± 0.2

Figure 5. K−M plot of different samples derived from its respective diffuse reflectance spectrum. Inset shows a magnified view of the absorption peaks in the region of 560−720 nm, indicating a shift in peak A. A, B, C, and D represent the characteristic excitonic absorption bands of 1L-MoS$_2$.

nm. Although the A and B peaks are associated with the optical absorption by the band-edge excitons, peaks C and D are associated with the van Hove singularities of MoS$_2$.[30] In the MoS$_2$@TiO$_2$ HS, besides the strong UV absorption by the TiO$_2$ core, all the characteristic MoS$_2$ absorbance peaks are detected with a much lower intensity, indicating the uniform growth of an atomically thin 1L-MoS$_2$ over TiO$_2$. It is noteworthy that peak A is observed to be slightly blue-shifted and detected at 657.1 nm, perhaps because of the quantum confinement effect as the layer number decreases from few layers to monolayer after the formation of HS with TiO$_2$.

3.3.2. PL Study. Figure 6a shows a comparison of the PL spectra of pristine 1L-MoS$_2$ and 1L-MoS$_2$@TiO$_2$ HS,
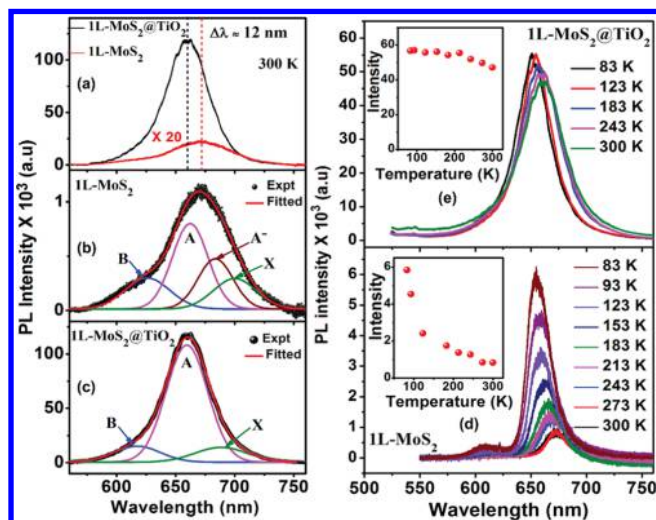

Figure 6. (a) Comparative PL spectra of the pristine 1L-MoS$_2$ and 1L-MoS$_2$@TiO$_2$ at room temperature. (b,c) Gaussian deconvolution of the PL spectra of pristine MoS$_2$ and MoS$_2$@TiO$_2$ HS, respectively, showing different excitonic peaks (A, B, A$^-$, and X). Low-temperature PL spectra for (d) pristine 1L-MoS$_2$ and (e) 1L-MoS$_2$@TiO$_2$ core−shell HS, recorded in the temperature range 83−300 K. The inset in each case shows the temperature dependence of the PL peak intensity.

measured at room temperature. The PL peak intensities for the pristine 1L-MoS$_2$ and 1L-MoS$_2$@TiO$_2$ HS are measured to be ∼1.5 and ∼120 K, respectively, in arbitrary units, as shown in Figure 6a. Thus, the formation of single-layer MoS$_2$ shell over the TiO$_2$ NRs provides about 80-fold or 2 orders of

magnitude enhancement in the PL intensity of 1L-MoS$_2$ compared to its pristine counterpart. Additionally, the PL spectrum was notably blue-shifted by ∼12 nm in case of HS, as compared to that of pristine 1L-MoS$_2$. To understand the origin of the PL emission, we have deconvoluted the spectra of the as-grown 1L-MoS$_2$ and 1L-MoS$_2$@TiO$_2$ HS by fitting them with a few Gaussian peaks: the neutral exciton (A), negative trion (A$^-$), B exciton, and the bound exciton (X) (Figure 6b,c). The summary of the spectral weight of each of the individual peaks for both the samples is presented in Table 1. The A exciton peak is derived from the direct band gap of MoS$_2$, whereas the B excitation peak arises from the direct band gap transition between the minima of the conduction band and the lower-level valence-band maxima, formed by the strong valence-band spin−orbit splitting at the K point in the Brillouin zone.[41] The A$^-$ exciton peak, which is understood as the transition from the trions, is caused by light n-type doping from the substrate or from the charged impurities in the CVD-grown 1L-MoS$_2$ film,[42] and the X exciton peak is attributed to the radiative recombination of the bound excitons.[43] Interestingly, after the formation of the HS, the spectral weight of A exciton peak increased from 41 to 76%, whereas that of the trion decreased from 23% to a negligible amount, as shown in Figure 6b,c and Table 1. The transition because of the defect-bound excitons (X) also decreases from ∼17 to ∼12% after the formation of HS, confirming the lower defect density in 1L-MoS$_2$ grown on TiO$_2$. When the heterojunction is formed between MoS$_2$ and TiO$_2$, the excess electrons present in the intrinsically n-type 1L-MoS$_2$ transfer to the TiO$_2$ side through the interface because of their special band arrangement, as shown in Figure S5 (Supporting Information).[36] Therefore, this depletion of excess electrons introduces p-type doping in 1L-MoS$_2$, as evidenced from the blue shift of the Raman and PL spectra, which switches the PL process from trion recombination to exciton recombination, leading to an enormous PL enhancement by the 1L-MoS$_2$ shell. On the other hand, the pristine TiO$_2$ NRs show a weak near-infrared PL emission band centered at ∼810 nm (see Figure S4, Supporting Information), which is attributed to the Ti-interstitial defects.[44] After the formation of MoS$_2$@TiO$_2$ HS, the intensity of the ∼810 nm peak increased marginally. This may be due to the recombination of excess electrons that migrate from MoS$_2$ to TiO$_2$.

The heterojunction between MoS$_2$ and TiO$_2$ usually forms a type-II HS, which facilitates an efficient transfer of the photoexcited electrons from the MoS$_2$ side to the TiO$_2$ side, resulting usually in PL quenching.[45] On the contrary, in our case, the charge transfer at the interface most likely occurs through the trions, that is, the excess electrons in the intrinsically n-type 1L-MoS$_2$, whereas the neutral excitons are not parted. This can be realized from the much higher binding energy of the neutral exciton (0.5−0.9 eV) than that of the trion (∼30 meV) generated in 1L-MoS$_2$ by photoexcitation. Thus, analogous to the typical chemical p-doping process, which converts light-inefficient trions to light-efficient excitons, it may be argued that the controlled interfacial charge transfer induces a p-doping effect, resulting in the giant enhancement of PL.[36] Additionally, the CVD growth process generally induces various structural defects in 1L-MoS$_2$. Thus, such structural defects in the 1L-MoS$_2$ shell grown by the CVD method over the TiO$_2$ core are expected, which is consistent with the STEM elemental composition showing a lower concentration of S, giving an indication of S vacancies.

Therefore, oxygen and water molecules adsorbed from the atmosphere can occupy the S vacancy sites, and/or oxygen in the TiO_2 lattice may form O−Mo−O or Mo═O bonding, which eventually introduces a p-type doping in the MoS_2 film, as compared to the pristine $1L-MoS_2$. Thus, we believe that the p-doping in the $1L-MoS_2@TiO_2$ HS leads to the conversion of negative trion to neutral exciton,[42] which enhances the PL intensity enormously.

To understand the relative contribution of the nonradiative and radiative processes, low-temperature PL measurements were carried out for both $1L-MoS_2$ and $1L-MoS_2@TiO_2$, and the results are shown in Figure 6d,e. It is clear that the PL intensity is considerably enhanced at low temperature for the pristine $1L-MoS_2$ sample. A 50× objective lens was used to focus the laser beam and to collect the PL signal at temperatures from 83 to 287 K in a low-temperature Linkam stage. The temperature dependence of PL intensity $I_{PL}(T)$ can be expressed by the equation[42,46]

$$I_{PL}(T) = \frac{I_{LT} \times K_{rad}(T)}{K_{rad}(T) + K_{nonrad}(T)}$$

where I_{LT} is the PL intensity at very low temperature, and $K_{rad}(T)$ and $K_{nonrad}(T)$ are the temperature-dependent radiative and nonradiative recombination rates, respectively. The nonradiative recombination rate is reported to be related to the defect-trapping rate and electron relaxation within the conduction and valence bands of a semiconductor.[41] Most of the semiconducting materials possess an extremely low quantum efficiency of emission at higher temperature because of the higher rate of nonradiative recombination activated with the thermal energy. In the present case, when the temperature increases from 83 to 300 K because of the nonradiative recombination, the PL intensity of the pristine $1L-MoS_2$ is reduced by ∼86%, as shown in Figure 6d and its inset. Surprisingly, the PL intensity of $1L-MoS_2@TiO_2$ HS is observed to be reduced to only by ∼17%, as shown in Figure 6e, with the increase of temperature to 300 K. Thus, it can be argued from the above equation that the nonradiative recombination rate of the excitons in the case of $1L-MoS_2@TiO_2$ HS is almost negligible and the PL emission is mostly dominated by radiative recombination.[42,47] This may also be one of the major reasons for the enormous PL enhancement at $1L-MoS_2$ in the $MoS_2@TiO_2$ HS. Further, it was observed that the nonradiative rate becomes nearly 7 times stronger than the radiative rate at room temperature for the case of pristine $1L-MoS_2$, whereas it is quite small for the HS sample. Thus, no significant quenching of PL is observed with the increase of temperature for the HS sample, which is very significant for its display application.

3.4. Effect of Oxygen Plasma Treatment. *3.4.1. Raman Study.* To have a more detailed understanding of the giant PL enhancement, oxygen plasma treatment was carried out for the pristine $1L-MoS_2$ and $1L-MoS_2@TiO_2$ HS for various time durations. Figure 7a shows the Raman spectra of the oxygen plasma-treated $1L-MoS_2$ sample irradiated up to 60 s. It is noteworthy to observe that the E_{2g} mode is not affected much, whereas the A_{1g} mode at ∼408 cm^{-1} is blue-shifted monotonically with an increase in the oxygen plasma exposure time. This is a clear indication of an effective p-doping in the MoS_2 lattice by oxygen bonding during the plasma treatment.[48] With the longer exposure of $1L-MoS_2$ to the oxygen plasma, the position of the A_{1g} peak does not shift further, but
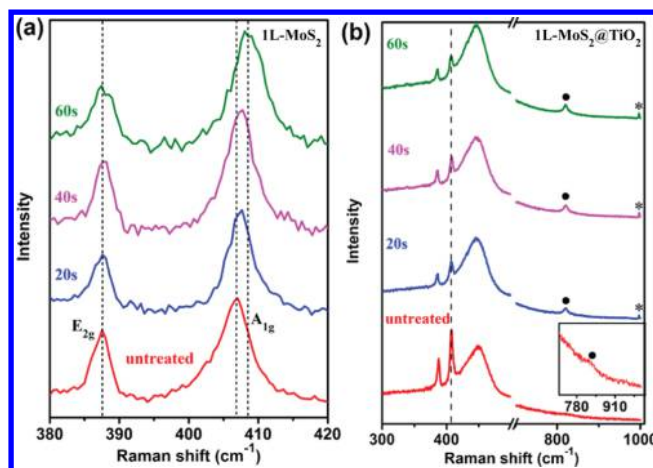

Figure 7. Raman spectra of oxygen plasma-treated (a) $1L-MoS_2$ and (b) $1L-MoS_2@TiO_2$ for different exposure times: 0−60 s. The vertical dotted lines in (a) indicate the shift in the Raman mode of MoS_2 with the plasma exposure time. The inset in (b) shows a magnified view of the spectrum for the untreated HS in the range of 740−1010 cm^{-1}. It reveals the evolution of the peak at ∼820 cm^{-1} (marked by symbol "●") after the plasma treatment.

the Raman intensity starts decreasing, implying the degradation of the film quality. Figure 7b shows the Raman spectra of the oxygen plasma-treated $1L-MoS_2@TiO_2$ HS for different durations of treatment (0−60 s). Note that because of the plasma treatment, the Raman peak intensity is gradually reduced with the plasma exposure time, though the peak positions for the E_{2g} and A_{1g} modes are unchanged. The reduced peak intensity signifies the gradual degradation of the MoS_2 film quality. Thus, after the growth of the $1L-MoS_2$ shell over the TiO_2 NRs, the MoS_2 layer becomes optimally p-doped, and no further doping is observed even after the oxygen plasma treatment. Interestingly, we observed a systematic increase in the peak intensity for a peak at ∼820 cm^{-1}, and an additional peak at ∼994 cm^{-1} is observed to be evolving with an increase in the plasma irradiation time, corresponding to the O−Mo−O and Mo═O bonds of molybdenum oxides (see Figure 7b).[40] These results clearly indicate the p-doping of the underlying MoS_2 layer in the HS sample.

3.4.2. PL Study. To further investigate the origin behind the strong PL enhancement in the $MoS_2@TiO_2$ HS, the PL spectra of both the pristine MoS_2 and $1L-MoS_2@TiO_2$ HS were recorded after oxygen plasma treatment for various time durations and analyzed. Figure 8a shows a comparison of the PL spectra for the pristine $1L-MoS_2$, before and after O_2 plasma treatment. The PL intensity is observed to be increased with the plasma exposure time up to 60 s, and then it decreases gradually, as shown in Figure 8b. Figure 8c,d shows the Gaussian deconvolution of the PL spectra of $1L-MoS_2$ after the oxygen plasma exposure for different time durations: 60 and 120 s, respectively. As the plasma irradiation is reported to introduce S-vacancies in the pristine $1L-MoS_2$,[43] the MoS_2 film is p-doped in the course of plasma treatment by the adsorption of oxygen molecules at the vacancy sites, which push away the electrons from the MoS_2. Therefore, the trion contribution is suppressed and hence the neutral exciton emission dominates, which results in the overall increase of the PL emission and the blue shift of the A exciton peak. When the irradiation time exceeds 60 s, we observed a systematic drop in the PL intensity (as shown in Figure 8b). Thus, at 60 s plasma irradiation, the
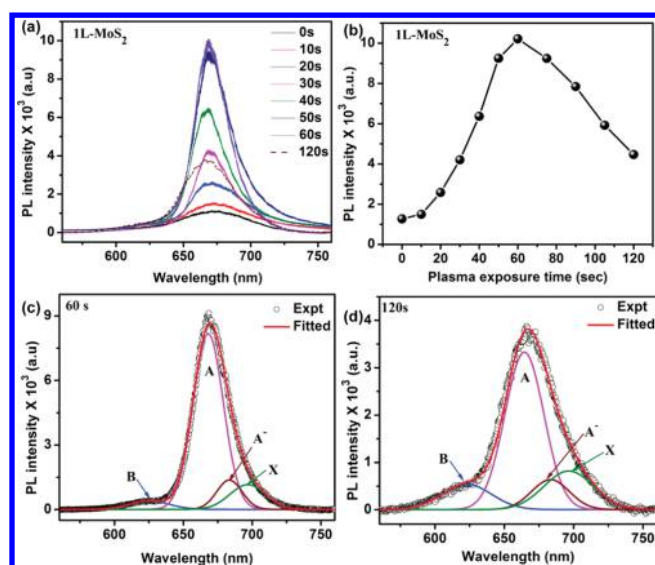
Figure 8. (a) Variation of PL spectra of 1L-MoS$_2$ as a function of the oxygen plasma exposure time duration. (b) The variation in PL intensity as a function of plasma exposure time. (c,d) Gaussiandeconvolution of the PL spectra of 1L-MoS$_2$, after 60 and 120 s of oxygen plasma treatment, respectively. The symbols for different fitted peaks are explained in the text.

Figure 9. (a) Comparison of the PL spectra of 1L-MoS$_2$@TiO$_2$ before and after oxygen plasma treatment for 30 and 60 s. (b) Change in PL intensity of MoS$_2$@TiO$_2$ with plasma exposure time. (c,d) Gaussian deconvolution of the PL spectra of oxygen plasma-treated (30 and 60 s, respectively) MoS$_2$@TiO$_2$. The symbols for different fitted peaks are explained in the text.

doping concentration may reach the optimum value, beyond which excessive defects are created by the plasma, which degrade the characteristic properties of MoS$_2$, consistent with the Raman analysis. After 120 s of plasma irradiation, the defect-induced X peak contribution is maximum in the PL peak, whereas the A and A$^-$ peaks decrease markedly in weight, as shown in Table 2.

Figure 9a depicts a comparison of the PL spectra of 1L-MoS$_2$@TiO$_2$ HS before and after oxygen plasma treatment for various time durations. With the increase in the plasma treatment time, the PL intensity decreased monotonically, as shown Figure 9b. To understand the change in spectral profile with plasma treatment, each spectrum was deconvoluted. Figure 9c,d shows the Gaussian deconvolution of the PL spectra for the oxygen plasma exposure times of 30 and 60 s, respectively. Because of the negligible contribution of trion A$^-$ in the as-grown MoS$_2$@TiO$_2$ HS (see Table 1), no significant conversion of A$^-$ to A exciton emission is observed in the HS after the plasma treatment. Therefore, the electron transfer-induced p-doping effect in the MoS$_2$ lattice may be discarded in case of the HS sample with the plasma exposure. Thus, it can be argued that the as-synthesized MoS$_2$@TiO$_2$ HS is optimally p-doped. However, the contribution of the defect-induced X peak increases substantially in the HS with the plasma treatment time, which implies the deterioration of the
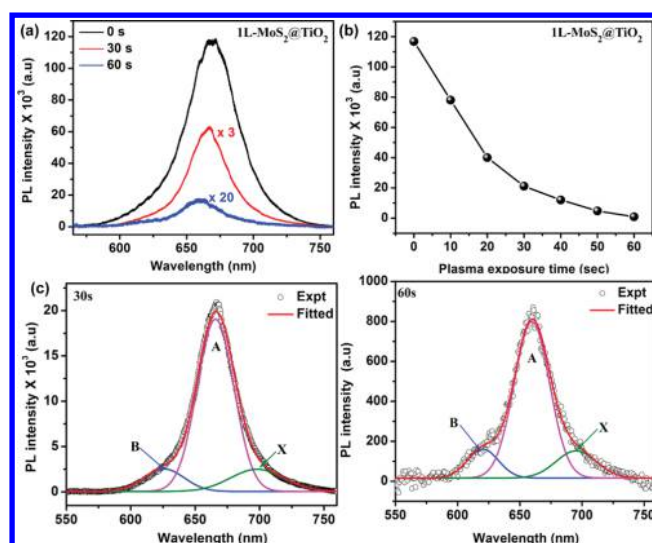
MoS$_2$ layer. As a result, the overall intensity goes down with the plasma exposure time in the case of the HS sample.

4. CONCLUSION

In summary, the 1L-MoS$_2$ shell was deposited by a direct CVD process on the hydrothermally grown vertical TiO$_2$ NRs, forming a MoS$_2$@TiO$_2$ core−shell structure. A strong enhancement in PL intensity (by nearly 2 orders of magnitude) at room temperature in the 1L-MoS$_2$@TiO$_2$ NR HS is demonstrated here. The formation of 1L-MoS$_2$@TiO$_2$ core−shell HS was confirmed by the Raman and HRTEM analyses. The observed strong PL enhancement is explained on the basis of oxygen-bonding-induced p-doping in MoS$_2$ lattice, which suppresses the trion emission and increases the neutral exciton emissions. The low-temperature PL measurement on the HS sample indicates the suppression of the nonradiative recombination of excitons at MoS$_2$, which eventually boosts the PL emission at room temperature. Finally, oxygen plasma irradiation was performed on the pristine MoS$_2$ and MoS$_2$@TiO$_2$ HS samples to verify p-doping through the oxygen bonding at the defect sites in MoS$_2$, resulting in the enhancement of PL. Our results provide a new and easy way to fabricate MoS$_2$-based HSs and tune the optical properties of MoS$_2$ to realize its practical applications in optoelectronic and nanophotonic devices.

Table 2. Evolution of the Different Peak Contributions to PL with the Oxygen Plasma Treatment for Different Time Durations in Pristine 1L-MoS$_2$ and MoS$_2$@TiO$_2$ HS

sample		B-exciton (B) (%)	A-exciton (A) (%)	trion (A$^-$) (%)	bound exciton (X) (%)
MoS$_2$	0 s	18.5 ± 0.7	40.8 ± 0.1	23.4 ± 0.5	17.3 ± 4.7
	60 s	4.7 ± 0.5	73.0 ± 0.1	10.2 ± 0.4	12.1 ± 0.1
	120 s	12.0 ± 0.4	58.8 ± 0.1	10.9 ± 0.9	18.3 ± 0.6
MoS$_2$@TiO$_2$	0 s	11.6 ± 0.2	76.3 ± 0.2	0	12.1 ± 0.2
	30 s	10.8 ± 0.5	75.1 ± 0.1	0	14.1 ± 0.5
	60 s	12.0 ± 1.3	73.5 ± 0.6	0	14.5 ± 2.7

■ ASSOCIATED CONTENT

ⓢ Supporting Information

The Supporting Information is available free of charge on the ACS Publications website at DOI: 10.1021/acs.jpcc.8b03957.

Schematic diagram of the experimental CVD setup for the growth of 1L-MoS$_2$; XRD patterns of TiO$_2$ NRs, MoS$_2$, and 1L-MoS$_2$@TiO$_2$ HS; magnified view of the Raman spectra with Lorentzian fits for pristine 1L-MoS$_2$ and 1L-MoS$_2$@TiO$_2$ HS; comparative PL spectra of TiO$_2$ and 1L-MoS$_2$@TiO$_2$ excited with 488 nm laser at room temperature; and schematic representation of the cross-sectional view of 1L-MoS$_2$@TiO$_2$ core–shell HS, showing the possible band arrangement and the interfacial charge transfer (PDF)

■ AUTHOR INFORMATION

Corresponding Author

*E-mail: giri@iitg.ernet.in.

ORCID ⬥

P. K. Giri: 0000-0003-2020-4249

Notes

The authors declare no competing financial interest.

■ ACKNOWLEDGMENTS

■ REFERENCES

(1) Du, X.; Skachko, I.; Barker, A.; Andrei, E. Y. Approaching Ballistic Transport in Suspended Graphene. *Nat. Nanotechnol.* **2008**, *3*, 491−495.

(2) Balandin, A. A.; Ghosh, S.; Bao, W.; Calizo, I.; Teweldebrhan, D.; Miao, F.; Lau, C. N. Superior Thermal Conductivity of Single-Layer Graphene. *Nano Lett.* **2008**, *8*, 902−907.

(3) Bolotin, K. I.; Sikes, K. J.; Jiang, Z.; Klima, M.; Fudenberg, G.; Hone, J.; Kim, P.; Stormer, H. L. Ultrahigh Electron Mobility in Suspended Graphene. *Solid State Commun.* **2008**, *146*, 351−355.

(4) Wang, Q. H.; Kalantar-Zadeh, K.; Kis, A.; Coleman, J. N.; Strano, M. S. Electronics and Optoelectronics of Two-Dimensional Transition Metal Dichalcogenides. *Nat. Nanotechnol.* **2012**, *7*, 699−712.

(5) Sundaram, R. S.; Engel, M.; Lombardo, A.; Krupke, R.; Ferrari, A. C.; Avouris, P.; Steiner, M. Electroluminescence in Single Layer Mos2. *Nano Lett.* **2013**, *13*, 1416−1421.

(6) Chow, P. K.; Jacobs-Gedrim, R. B.; Gao, J.; Lu, T.-M.; Yu, B.; Terrones, H.; Koratkar, N. Defect-Induced Photoluminescence in Monolayer Semiconducting Transition Metal Dichalcogenides. *ACS Nano* **2015**, *9*, 1520−1527.

(7) Yang, S.; et al. Self-Driven Photodetector and Ambipolar Transistor in Atomically Thin GaTe-MoS2 p-n vdW Heterostructure. *ACS Appl. Mater. Interfaces* **2016**, *8*, 2533−2539.

(8) Lee, H. S.; Min, S.-W.; Chang, Y.-G.; Park, M. K.; Nam, T.; Kim, H.; Kim, J. H.; Ryu, S.; Im, S. Mos2 Nanosheet Phototransistors with Thickness-Modulated Optical Energy Gap. *Nano Lett.* **2012**, *12*, 3695−3700.

(9) Radisavljevic, B.; Radenovic, A.; Brivio, J.; Giacometti, V.; Kis, A. Single-Layer Mos2 Transistors. *Nat. Nanotechnol.* **2011**, *6*, 147−150.

(10) Mak, K. F.; Lee, C.; Hone, J.; Shan, J.; Heinz, T. F. Atomically Thin Mos_2: A New Direct-Gap Semiconductor. *Phys. Rev. Lett.* **2010**, *105*, 136805.

(11) Sarkar, D.; Xie, X.; Liu, W.; Cao, W.; Kang, J.; Gong, Y.; Kraemer, S.; Ajayan, P. M.; Banerjee, K. A Subthermionic Tunnel Field-Effect Transistor with an Atomically Thin Channel. *Nature* **2015**, *526*, 91−95.

(12) Mak, K. F.; He, K.; Lee, C.; Lee, G. H.; Hone, J.; Heinz, T. F.; Shan, J. Tightly Bound Trions in Monolayer Mos2. *Nat. Mater.* **2012**, *12*, 207−211.

(13) Ross, J. S.; et al. Electrical Control of Neutral and Charged Excitons in a Monolayer Semiconductor. *Nat. Commun.* **2013**, *4*, 1474.

(14) Dhakal, K. P.; Duong, D. L.; Lee, J.; Nam, H.; Kim, M.; Kan, M.; Lee, Y. H.; Kim, J. Confocal Absorption Spectral Imaging of Mos2: Optical Transitions Depending on the Atomic Thickness of Intrinsic and Chemically Doped Mos2. *Nanoscale* **2014**, *6*, 13028−13035.

(15) Kime, G.; Leontiadou, M. A.; Brent, J. R.; Savjani, N.; O'Brien, P.; Binks, D. Ultrafast Charge Dynamics in Dispersions of Monolayer Mos2 Nanosheets. *J. Phys. Chem. C* **2017**, *121*, 22415−22421.

(16) Ross, J. S.; et al. Electrically tunable excitonic light-emitting diodes based on monolayer WSe2 p-n junctions. *Nat. Nanotechnol.* **2014**, *9*, 268−272.

(17) Mouri, S.; Miyauchi, Y.; Matsuda, K. Tunable Photoluminescence of Monolayer Mos2 Via Chemical Doping. *Nano Lett.* **2013**, *13*, 5944−5948.

(18) Park, S.; Kim, M. S.; Kim, H.; Lee, J.; Han, G. H.; Jung, J.; Kim, J. Spectroscopic Visualization of Grain Boundaries of Monolayer Molybdenum Disulfide by Stacking Bilayers. *ACS Nano* **2015**, *9*, 11042−11048.

(19) Kim, M. S.; Seo, C.; Kim, H.; Lee, J.; Luong, D. H.; Park, J.-H.; Han, G. H.; Kim, J. Simultaneous Hosting of Positive and Negative Trions and the Enhanced Direct Band Emission in Mose2/Mos2 Heterostacked Multilayers. *ACS Nano* **2016**, *10*, 6211−6219.

(20) Tang, K.; Qi, W.; Li, Y.; Wang, T. Electronic Properties of Van Der Waals Heterostructure of Black Phosphorus and Mos2. *J. Phys. Chem. C* **2018**, *122*, 7027−7032.

(21) Qiu, H.; et al. Hopping Transport through Defect-Induced Localized States in Molybdenum Disulphide. *Nat. Commun.* **2013**, *4*, 2642.

(22) van der Zande, A. M.; Huang, P. Y.; Chenet, D. A.; Berkelbach, T. C.; You, Y.; Lee, G.-H.; Heinz, T. F.; Reichman, D. R.; Muller, D. A.; Hone, J. C. Grains and Grain Boundaries in Highly Crystalline Monolayer Molybdenum Disulphide. *Nat. Mater.* **2013**, *12*, 554−561.

(23) Cunningham, P. D.; McCreary, K. M.; Hanbicki, A. T.; Currie, M.; Jonker, B. T.; Hayden, L. M. Charge Trapping and Exciton Dynamics in Large-Area Cvd Grown Mos2. *J. Phys. Chem. C* **2016**, *120*, 5819−5826.

(24) Zeng, Y.; Li, X.; Chen, W.; Liao, J.; Lou, J.; Chen, Q. Highly Enhanced Photoluminescence of Monolayer Mos2 with Self-Assembled Au Nanoparticle Arrays. *Adv. Mater. Interfaces* **2017**, *4*, 1700739.

(25) Sobhani, A.; Lauchner, A.; Najmaei, S.; Ayala-Orozco, C.; Wen, F.; Lou, J.; Halas, N. J. Enhancing the Photocurrent and Photoluminescence of Single Crystal Monolayer Mos2 with Resonant Plasmonic Nanoshells. *Appl. Phys. Lett.* **2014**, *104*, 031112.

(26) Ghimire, G.; Adhikari, S.; Jo, S. G.; Kim, H.; Jiang, J.; Joo, J.; Kim, J. Local Enhancement of Exciton Emission of Monolayer Mos2 by Copper Phthalocyanine Nanoparticles. *J. Phys. Chem. C* **2018**, *122*, 6794−6800.

(27) Paul, K. K.; Ghosh, R.; Giri, P. K. Mechanism of strong visible light photocatalysis by Ag2O-nanoparticle-decorated monoclinic TiO2(B) porous nanorods. *Nanotechnology* **2016**, *27*, 315703.

(28) Paul, K. K.; Giri, P. K. Role of Surface Plasmons and Hot Electrons on the Multi-Step Photocatalytic Decay by Defect Enriched Ag@Tio2 Nanorods under Visible Light. *J. Phys. Chem. C* **2017**, *121*, 20016−20030.

(29) Tan, Y.-H.; Yu, K.; Li, J.-Z.; Fu, H.; Zhu, Z.-Q. Mos2@Zno Nano-Heterojunctions with Enhanced Photocatalysis and Field Emission Properties. *J. Appl. Phys.* **2014**, *116*, 064305.

(30) Sun, Y.; Lin, H.; Wang, C.; Wu, Q.; Wang, X.; Yang, M. Morphology-Controlled Synthesis of Tio2/Mos2 Nanocomposites

with Enhanced Visible-Light Photocatalytic Activity. *Inorg. Chem. Front.* **2018**, *5*, 145−152.

(31) Chen, B.; Meng, Y.; Sha, J.; Zhong, C.; Hu, W.; Zhao, N. Preparation of Mos2/Tio2 Based Nanocomposites for Photocatalysis and Rechargeable Batteries: Progress, Challenges, and Perspective. *Nanoscale* **2018**, *10*, 34−68.

(32) Mondal, S.; Basak, D. Very high photoresponse towards low-powered UV light under low-biased condition by nanocrystal assembled TiO 2 film. *Appl. Surf. Sci.* **2018**, *427*, 814−822.

(33) Mondal, S.; Basak, D. Defect controlled tuning of the ratio of ultraviolet to visible light emission in TiO 2 thin films. *J. Lumin.* **2016**, *179*, 480−486.

(34) Sarkar, S.; Basak, D. Self Powered Highly Enhanced Dual Wavelength ZnO@CdS Core-Shell Nanorod Arrays Photodetector: An Intelligent Pair. *ACS Appl. Mater. Interfaces* **2015**, *7*, 16322−16329.

(35) Paul, K. K.; Giri, P. K. Plasmonic Metal and Semiconductor Nanoparticle Decorated Tio2-Based Photocatalysts for Solar Light Driven Photocatalysis A2-Wandelt, Klaus. *Encyclopedia of Interfacial Chemistry*; Elsevier: Oxford, 2018; pp 786−794.

(36) Kim, M. S.; Roy, S.; Lee, J.; Kim, B. G.; Kim, H.; Park, J.-H.; Yun, S. J.; Han, G. H.; Leem, J.-Y.; Kim, J. Enhanced Light Emission from Monolayer Semiconductors by Forming Heterostructures with Zno Thin Films. *ACS Appl. Mater. Interfaces* **2016**, *8*, 28809−28815.

(37) Mohapatra, P. K.; Deb, S.; Singh, B. P.; Vasa, P.; Dhar, S. Strictly Monolayer Large Continuous Mos2 Films on Diverse Substrates and Their Luminescence Properties. *Appl. Phys. Lett.* **2016**, *108*, 042101.

(38) Li, H.; Zhang, Q.; Yap, C. C. R.; Tay, B. K.; Edwin, T. H. T.; Olivier, A.; Baillargeat, D. From Bulk to Monolayer Mos2: Evolution of Raman Scattering. *Adv. Funct. Mater.* **2012**, *22*, 1385−1390.

(39) Chakraborty, B.; Bera, A.; Muthu, D. V. S.; Bhowmick, S.; Waghmare, U. V.; Sood, A. K. Symmetry-Dependent Phonon Renormalization in Monolayer Mos${}_{2}$ Transistor. *Phys. Rev. B: Condens. Matter Mater. Phys.* **2012**, *85*, 161403.

(40) Pang, Q.; Zhao, Y.; Bian, X.; Ju, Y.; Wang, X.; Wei, Y.; Liu, B.; Du, F.; Wang, C.; Chen, G. Hybrid Graphene@Mos2@Tio2 Microspheres for Use as a High Performance Negative Electrode Material for Lithium Ion Batteries. *J. Mater. Chem. A* **2017**, *5*, 3667−3674.

(41) Splendiani, A.; Sun, L.; Zhang, Y.; Li, T.; Kim, J.; Chim, C.-Y.; Galli, G.; Wang, F. Emerging Photoluminescence in Monolayer Mos2. *Nano Lett.* **2010**, *10*, 1271−1275.

(42) Nan, H.; et al. Strong Photoluminescence Enhancement of Mos2 through Defect Engineering and Oxygen Bonding. *ACS Nano* **2014**, *8*, 5738−5745.

(43) Tongay, S.; et al. Defects Activated Photoluminescence in Two-Dimensional Semiconductors: Interplay between Bound, Charged, and Free Excitons. *Sci. Rep.* **2013**, *3*, 2657.

(44) Santara, B.; Giri, P. K.; Imakita, K.; Fujii, M. Microscopic Origin of Lattice Contraction and Expansion in Undoped Rutile Tio 2 Nanostructures. *J. Phys. D: Appl. Phys.* **2014**, *47*, 215302.

(45) Zhou, W.; Yin, Z.; Du, Y.; Huang, X.; Zeng, Z.; Fan, Z.; Liu, H.; Wang, J.; Zhang, H. Synthesis of Few-Layer MoS2Nanosheet-Coated TiO2Nanobelt Heterostructures for Enhanced Photocatalytic Activities. *Small* **2013**, *9*, 140−147.

(46) Gaponenko, M. S.; Lutich, A. A.; Tolstik, N. A.; Onushchenko, A. A.; Malyarevich, A. M.; Petrov, E. P.; Yumashev, K. V. Temperature-Dependent Photoluminescence of Pbs Quantum Dots in Glass: Evidence of Exciton State Splitting and Carrier Trapping. *Phys. Rev. B: Condens. Matter Mater. Phys.* **2010**, *82*, 125320.

(47) Feldmann, J.; Peter, G.; Göbel, E. O.; Dawson, P.; Moore, K.; Foxon, C.; Elliott, R. J. Linewidth Dependence of Radiative Exciton Lifetimes in Quantum Wells. *Phys. Rev. Lett.* **1987**, *59*, 2337−2340.

(48) Wei, X.; Yu, Z.; Hu, F.; Cheng, Y.; Yu, L.; Wang, X.; Xiao, M.; Wang, J.; Wang, X.; Shi, Y. Mo-O Bond Doping and Related-Defect Assisted Enhancement of Photoluminescence in Monolayer Mos2. *AIP Adv.* **2014**, *4*, 123004.